Nanoscale

ROYAL SOCIETY OF CHEMISTRY

PAPER

View Article Online
View Journal | View Issue

Cite this: *Nanoscale*, 2025, **17**, 13258

Multivariate chemometric design of nitric oxide-releasing chitosan nanoparticles for skin-related biomedical applications†

Renan S. Nunes, * Victor D. P. Cinel, Joana C. Pieretti, Kelli C. F. Mariano, Roberta A. dos Reis, Morgana Halfeld and Amedea B. Seabra *

Received 11th March 2025,
Accepted 8th May 2025

DOI: 10.1039/d5nr01044f

rsc.li/nanoscale

Nitric oxide (NO) is a critical signaling molecule with significant therapeutic potential for biomedical applications, particularly in wound healing, antimicrobial activity, and tissue repair. However, its clinical translation is hindered by its instability and rapid degradation in biological environments. In this study, we employed chemometric techniques to optimize the synthesis of glutathione-loaded chitosan nanoparticles (GSH-CSNPs) produced *via* ionotropic gelation. GSH serves as a precursor molecule for *S*-nitrosoglutathione (GSNO), a key NO donor. A multivariate experimental design was applied to systematically investigate eight synthesis parameters, optimizing particle size, polydispersity index (PDI), zeta potential (ZP), stability, storage conditions, and NO release kinetics. The optimized nanoparticles exhibited a hydrodynamic diameter of 77.1 ± 1.5 nm, a PDI of 0.209 ± 0.010, and a ZP of +15.3 ± 2.1 mV, ensuring considerable colloidal stability for at least 60 days at room temperature. NO release kinetics demonstrated a sustained and controlled release profile from GSNO-CSNPs compared to free GSNO, enhancing NO availability. Franz permeation cell assays revealed efficient GSNO permeation through synthetic skin membranes, and *in vitro* cytotoxicity assays using human fibroblast cells confirmed the biocompatibility of GSNO-CSNPs up to a NO donor concentration of 250 μmol L^{-1}. Additionally, *S*-nitrosylated protein quantification in FN1 cells showed that GSNO-CSNPs at 500 μM induced a significant increase in *S*-nitrosylation levels, approximately 3 fold-higher than free GSNO at the same concentration, without a corresponding increase in cytotoxicity. This suggests that CSNPs enhance intracellular GSNO delivery, facilitating protein *S*-nitrosylation while maintaining cell viability. These findings highlight the pivotal role of Design of Experiments (DoE)-driven optimization in fine-tuning nanoparticle properties, providing a deeper understanding of how synthesis parameters influence their characteristics, and ultimately enhancing NO delivery systems for biomedical applications, particularly in skin-related therapies.

1. Introduction

Nitric oxide (NO) is a signaling molecule that plays a critical role in various physiological processes. Some examples are vasodilation,[1] immune modulation,[2] antimicrobial activity,[3] antiprotozoal activity,[4] wound healing and tissue regeneration,[5–8] and anticancer activity.[9,10] Nevertheless, as a free radical, NO is unstable, with a short half-life in biological systems due to its rapid oxidation and reactivity with other molecules.[11] This instability poses significant challenges for its exogenous application in biomedical therapies, as it requires controlled delivery to maintain efficacy while minimizing off-target effects.[12] To overcome this, various NO donors, such as *S*-nitrosothiols, diazeniumdiolates, and metal nitrosyl complexes, have been developed to provide sustained NO release. However, these donors often face limitations, including uncontrolled release rates, potential cytotoxicity, and systemic effects in off-target sites, which can hinder their clinical translation.[13,14] Among the NO donors, *S*-nitrosothiols (RSNOs), such as *S*-nitrosoglutathione (GSNO), have been successfully used as NO donors in several biomedical applications. GSNO undergoes spontaneous decomposition, yielding NO and GS-SG (oxidized GSH), without the formation of toxic molecules.[15,16] Indeed, GSNO possesses several biological effects attributed to NO itself, such as local vasodilation[17] and wound repair.[18]

In the last years, NO-releasing nanomaterials have garnered significant attention for their potential in drug delivery and

Center for Natural and Human Sciences, Federal University of ABC (UFABC), Santo André, SP, 09210-580, Brazil. E-mail: amedea.seabra@ufabc.edu.br, r.nunes@ufabc.edu.br

† Electronic supplementary information (ESI) available. See DOI: https://doi.org/10.1039/d5nr01044f

therapeutic systems, particularly in dermatological applications.[19,20] In this context, NO-releasing chitosan nanoparticles (CSNPs) emerge as an innovative solution, offering not only the biocompatibility, biodegradability, and antimicrobial activity of chitosan but also the ability to enhance, stabilize, and sustain NO release, addressing its inherent limitations.[21] CSNPs produced *via* the ionotropic gelation method offer additional benefits, such as simplicity of synthesis, cost-effectiveness, and their inherent positive charge, which facilitates interactions with negatively charged biological tissues, including the skin.[22] Our research group has previously demonstrated the effectiveness of NO-releasing CSNPs in several biomedical applications, such as the development of antileishmanial platforms,[23] treatment of cutaneous leishmaniasis,[24] toxicity against *Trypanosoma Cruzi*,[25] antibacterial activity,[26] and transdermal NO delivery.[27] Therefore, these characteristics make CSNPs particularly appealing for large-scale industrial production and several applications, aligning with the economic and practical demands of pharmaceutical manufacturing.

Despite promising results reported in the literature, a significant gap remains in understanding the factors that influence the physicochemical properties and long-term stability of CSNPs, particularly concerning variations in synthesis conditions. This gap poses a challenge for translating these technologies into industrial-scale production, as inconsistent properties, such as low reproducibility, highly-variable sizes, and high polydispersity index (PDI), can hinder their suitability for biomedical applications. Regulatory guidelines established in the United States, Europe, and South America, emphasize the importance of achieving low PDI values for the development of consistent, reliable, and high-quality nanomedicines.[28–30] For instance, small nanoparticles are reported to exhibit enhanced skin penetration, improved bioavailability, and a superior ability to evade the immune system, reducing clearance and extending their circulation time, which is advantageous for achieving controlled and sustained NO-based therapies within biological environments.[31–33] In addition, these regulatory agencies advocate for the implementation of Design of Experiments (DoE) and Quality by Design (QbD) principles for producing pharmaceutical products, which facilitate the systematic optimization of synthesis parameters and process controls, ensuring robust manufacturing processes and consistent product characteristics tailored for therapeutic applications.[34,35] DoE is particularly advantageous as it significantly reduces the number of experiments required to achieve optimal formulations, making it an essential tool for resource-efficient research and development. Complex systems that would otherwise require years of experimental iteration or be practically infeasible due to limitations in time, cost, and material availability can be systematically investigated and optimized in a fraction of the time.[36,37]

To advance NO-releasing CSNPs as viable biomedical products, it is essential to thoroughly investigate the factors influencing their properties, understand their impact on performance, and establish methods to control these parameters. By consistently producing nanoparticles with desirable characteristics—such as small size, low PDI, and stable NO release profiles—the therapeutic potential of CSNPs can be fully realized, paving the way for their successful application in clinical settings.

In this study, we employed advanced chemometric techniques, including DoE, to optimize the synthesis of NO-releasing CSNPs, ensuring controlled physicochemical properties such as particle size, PDI, stability, storage conditions, and NO release kinetics. By applying multivariate experimental designs, we systematically evaluated the influence of several synthesis parameters on nanoparticle characteristics, leading to an optimized formulation with enhanced stability and controlled NO release. While previous studies have explored NO release from CSNPs, our work uniquely integrates chemometric modeling to optimize formulation parameters, thereby improving reproducibility, scalability, and performance. This approach allows for precise control over nanoparticle characteristics, addressing major limitations in the field, such as inconsistent synthesis outcomes and unpredictable NO release profiles. Additionally, to our best knowledge, this is the first report to utilize DoE for tailoring NO-releasing CSNPs for biomedical applications, providing a robust methodological framework that can be extended to other biomedical applications requiring controlled NO delivery. These findings highlight the potential of integrating nanotechnology with data-driven optimization strategies to advance NO-based therapies in a reproducible and scalable manner.

2. Materials and methods

2.1. Materials

Chitosan (low molecular weight, ≥75% deacetylated, Sigma-Aldrich, Code: 448869-50G, Source: BCCL2629, viscosity of a 1% (w/v) chitosan solution in 1% (w/v) acetic acid = 136 cps), sodium tripolyphosphate (TPP), glutathione (GSH), sodium nitrite ($NaNO_2$), RPMI 1640 medium, fetal bovine serum, and dimethyl sulfoxide (DMSO) were purchased from Sigma-Aldrich (St Louis, MO, USA). Acetic acid (≥99%), Sodium chloride (NaCl), monopotassium phosphate (KH_2PO_4), dipotassium phosphate (K_2HPO_4), sodium hydroxide (NaOH), and hydrochloric Acid (HCl) were obtained from Labsynth (Diadema, SP, Brazil). Penicillin/streptomycin antibiotics were obtained from Gibco (USA). Strat-M® membrane was purchased from Merck (Darmstadt, Germany). Ultrapure water (Milli-Q) was used in all experiments.

2.2. GSH-CSNPs synthesis

GSH (the NO donor precursor molecule)-loaded chitosan nanoparticles (GSH-CSNPs) were produced at room temperature using the ionotropic gelation method, chosen for its low cost, simplicity, and compatibility with industrial-scale manufacturing techniques.[24,38] In a typical process, appropriate amounts of CS and NaCl (to control the ionic strength of the medium) were dissolved in 50 mL of an aqueous acetic acid

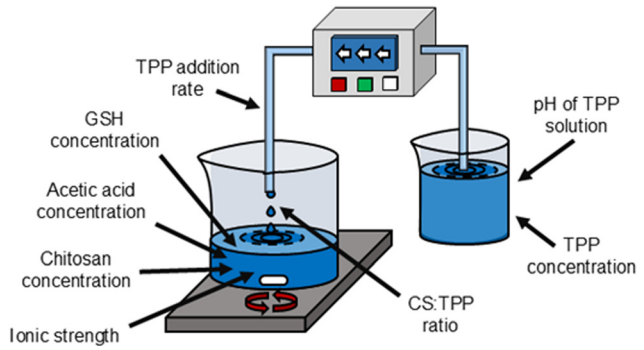

Fig. 1 Schematic representation of the experimental setup for GSH-CSNP production, highlighting the key process variables investigated.

solution for 1 hour. The resulting solution was centrifuged at 2.5 RCF for 10 minutes, and 40 mL of the supernatant was transferred to a 100 mL beaker using a pipette to remove any remaining solid particles. Subsequently, GSH was dissolved in the previously described solution. Then, a TPP solution with pre-adjusted pH was added dropwise at a controlled flow rate into the CS/GSH solution under stirring at 500 rpm (using a 2.5 cm magnetic stir bar) until the desired CS : TPP ratio was achieved. The stirring speed was carefully selected to ensure maximum agitation within the flask without generating bubbles, which could interfere with the homogeneity of the process. The addition was performed with a peristaltic pump (MPV-500, Marte Scientific®, Brazil) equipped with an inert Tygon® tube (internal diameter: 1.42 mm). After the TPP addition was complete, the system was stirred for an additional hour to complete the reticulation process. The nanoparticle suspensions were then stored in polypropylene conical tubes, kept in the dark, for further testing and characterization. Fig. 1 illustrates the experimental setup used for GSH-CSNPs production and the variables investigated.

2.3. Chemometric methods

The production process parameters for the nanoparticles were investigated and optimized using multivariate experimental design techniques. A two-step sequential approach was employed: first, a Plackett–Burman design was used to screen for the most influential variables; then, a Face-Centered Design (FCD) was applied to optimize the significant parameters identified in the initial screening. These parameters were selected based on the outcomes of the first design. Further details of both experimental designs are provided in the following sections.

2.3.1. Plackett–Burman design for identifying key factors of the synthesis. The Plackett–Burman design was employed to investigate 8 distinct parameters in the synthesis of the nanoparticles, which were selected after an extensive review of related works reported in literature:[39–43] (1) chitosan concentration, (2) TPP solution concentration, (3) TPP solution addition rate, (4) pH of the TPP solution, (5) CS : TPP ratio, (6) GSH concentration, (7) acetic acid concentration, and (8) additional ionic strength of the medium. The objective of this design was to identify which variables had the most significant impact on the properties of the nanoparticles, in order to select them for further optimization in the next phase of the synthesis process.

Table 1 Factors and levels investigated in the Plackett–Burman design

			Levels		
Factor		Unit	−1	0	+1
X_1	Initial chitosan concentration	mg mL^{-1}	0.5	1.3	2.1
X_2	TPP solution concentration	mg mL^{-1}	1.0	3.0	5.0
X_3	TPP solution addition rate	µL min^{-1}	50	100	150
X_4	pH of TPP solution	—	6	7.5	9
X_5	CS : TPP mass ratio	g_{CS} g_{TPP}^{-1}	1.5	3.25	5.0
X_6	Final GSH concentration	mmol L^{-1}	25	62.5	100
X_7	Initial acetic acid concentration	% m V^{-1}	0.5	1.0	1.5
X_8	Additional ionic strength	mmol L^{-1}	0	25	50

The ranges investigated for each variable are listed in Table 1, and the experimental matrix containing all the experiments performed is provided in Table S1.† The acetic acid concentration used in the synthesis indirectly modulates the pH of the medium, which in turn affects chitosan protonation and its electrostatic interaction with TPP. The tested concentrations (0.5–1.5% w/v) correspond to an estimated pH range of 3.0 to 4.0 after the dissolution and protonation of CS. Broader pH variation was not explored in this specific study for three main reasons: (i) higher pH values reduce chitosan protonation and result in particle destabilization; (ii) the nitrosation of GSH to form GSNO occurs efficiently only in acidic media (pH 3 to 4); and (iii) excessively acidic environments compromise biological compatibility and may promote premature hydrolysis of TPP. Therefore, the chosen pH range represents an optimal compromise between particle formation, functionalization, and biomedical applicability.

A Plackett–Burman matrix with 12 experimental runs and 3 center points was used, resulting in a total of 15 experiments. The data obtained were processed and analyzed using Design-Expert 13 software (Stat-Ease), with a significance level of α = 0.1 (90% confidence) for the statistical analyses.

The responses used in the Plackett–Burman design to evaluate the obtained materials included average size, PDI, and ZP, measured immediately post-synthesis and over time, with suspensions stored either at room temperature (20 °C) or under refrigeration (4 °C) at 1-, 7-, and 30 days post-synthesis. The response matrix, containing the numerical values for each response across all experiments, is provided in Table S2.† These responses were selected to investigate key physicochemical properties of the nanoparticles. Details on the methods used to measure the responses mentioned are described in the section 2.4.

2.3.2. Face-centered design for refinement and optimization. Based on the findings from the Plackett–Burman design, a Face-Centered Design (FCD) was utilized to further investigate and optimize two key parameters in nanoparticle synthesis: (1) the CS : TPP mass ratio and (2) the final GSH

Table 2 Factors and levels investigated in the face centered design

Factor		Unit	Levels[a]		
			−1	0	+1
X_1	CS : TPP mass ratio	$g_{CS}\ g_{TPP}^{-1}$	1.5	2.25	3
X_2	Final GSH concentration	mmol L^{-1}	20	30	40

[a] Fixed variables: initial chitosan concentration = 0.5 mg mL^{-1}; TPP solution concentration = 1 mg mL^{-1}; TPP solution addition rate = 0.1 mL min^{-1}; pH of TPP solution ≈ 9.0; initial acetic acid concentration = 1.5% m V^{-1}; additional ionic strength = 0 mmol L^{-1} (absence of NaCl).

concentration. The ranges investigated for each variable are listed in Table 2, and the experimental matrix containing all the experiments performed is provided in Table S3.† A FCD matrix with 8 experimental runs and 3 center points was used, resulting in a total of 11 experiments. The data obtained were processed and analyzed using Design-Expert 13 software (Stat-Ease), with a significance level of $\alpha = 0.05$ (95% confidence) for the statistical analyses. The responses analyzed in the Face-Centered Design (FCD) were the same as those evaluated in the Plackett–Burman design and are shown in Table S4.†

2.4. Characterization of NPs

The Dynamic Light Scattering (DLS) parameters of the GSH-CSNPs were measured using a DTS1070 cuvette with a Zetasizer Nano ZS (Malvern Panalytical, UK). Measurements were conducted at 20 °C with a backscatter detection angle of 173°. Each sample was measured in triplicate to ensure reproducibility. The results were reported as the average hydrodynamic diameter, polydispersity index (PDI), and zeta potential (ZP), with size distributions based on intensity to facilitate the detection of potential aggregates. For High-Resolution Transmission Electron Microscopy (HRTEM) analysis, samples were dispersed in ultrapure water (Milli-Q) and an aliquot of 10 μL of the suspension was drop-cast onto a carbon-coated copper TEM grid and allowed to dry at room temperature. Imaging was performed using a Talos F200X G2 HRTEM (Thermo Fisher Scientific, USA).

2.5. NO release kinetics from GSH-CSNPs

To obtain the NO donor molecule (GSNO), GSH molecules in the CSNP suspensions were nitrosated by adding equimolar amounts of $NaNO_2$, related to GSH, to the GSH-CSNPs suspensions. During this process, the thiol groups of GSH are nitrosated in acidic media to form GSNO (eqn (1)), which subsequently decomposes spontaneously over time, releasing NO (eqn (2)).[24] The formation of GSNO into CSNPs was confirmed by the detection of GSNO characteristic absorption band at 545 nm, with molar absorptivity coefficient of 18 L mol^{-1} cm, associated with $n_N \rightarrow \pi^*$ transition.[44,45]

$$GSH_{(aq)} + {NO_2}^-{}_{(aq)} + {H^+}_{(aq)} \rightarrow GSNO_{(aq)} + H_2O_{(l)} \quad (1)$$

$$2\ GSNO_{(aq)} \rightarrow GS\text{-}SG_{(aq)} + 2\ NO_{(g)} \quad (2)$$

The kinetics of NO release from GSNO were monitored by measuring absorbance changes at 545 nm (using an Agilent Synergy H1 Plate Reader). The decay of this absorption band corresponds to S–N cleavage with free NO release.[46] In a typical experiment, aliquots of the GSH-CSNP suspensions were transferred to a 96-well plate, diluted with 1.5% (w/v) acetic acid, and nitrosated by adding a 100 mmol L^{-1} $NaNO_2$ solution equimolar to the initial GSH concentration. To ensure consistency between experimental groups, all kinetic experiments were performed with an initial GSH concentration of 15 mmol L^{-1}. Data were collected at 37 °C (physiological temperature) over a 7 hour period, with readings taken at 20 minute intervals under double orbital agitation. Each experiment was conducted in triplicates. Additionally, kinetic data for free GSNO (without CSNPs), obtained after nitrosation of free GSH molecules, were obtained as a control in the same conditions of the GSH-CSNPs.

2.6. *In vitro* GSNO permeation assay

Franz permeation cells were used for GSNO permeation assays from optimized GSH-CSNPs after GSH nitrosation. The initial concentration of the NO donor was 30 mmol L^{-1}. The donor compartment (1 mL) contained the GSH-CSNPs (30 mmol L^{-1} of GSH, which was converted to GSNO after nitrosation), while the receptor compartment (7 mL) held potassium phosphate buffer (pH 5.5, 0.01 M KH_2PO_4). The assay was conducted at 32.5 °C, mimicking skin conditions. The Strat-M® membrane was used for drug permeation studies. Aliquots (1 mL) were collected from the receptor compartment at 30, 60, and 45 minutes, then hourly up to 8 hours, with a final sample at 24 hours. GSNO detection was performed *via* UV-Vis spectrophotometry (Agilent 8454) at 336 nm (ε = 980 mol L^{-1} cm). This absorption band corresponds to the S–N bond ($\pi \rightarrow \pi^*$ transition)[44,45] data analysis employed the zero-order, Higuchi, Korsmeyer-Peppas, and Hixson–Crowell models, according to previously established protocol.[47] Experiments were performed in triplicates, and data were analyzed *via* one-way ANOVA using the software GraphPad Prism 8.0.2.

2.7. Human cell culture

The non-tumoral human fibroblast FN1 cells used in this study, obtained from the Cell Bank of the Instituto Butantan (São Paulo, SP, Brazil), were cultured in RPMI 1640 medium supplemented with 10% fetal bovine serum and 1% penicillin/streptomycin antibiotics. The cells were maintained in an incubator at 37 °C with 5% CO_2, and their maintenance involved subculturing whenever they reached approximately 70% of confluence.

2.8. Cell viability assay

The MTT assay was used to evaluate cell viability. For this analysis, FN1 cells were seeded into a 96-well culture plate at a density of 1.0×10^4 cells per well. After 24 hours, the medium was replaced with fresh medium containing blank CSNPs (empty nanoparticles), GSNO-CSNPs, or free GSNO (non-encapsulated GSNO). The formulations were tested with NO

donor concentrations ranging from 5 to 500 μmol L^{-1}. Blank CSNPs were added in an amount equivalent to the CSNPs containing the NO donor, ensuring the same dosage. As a positive control for cell viability decrease, 5% DMSO was used, while as a negative control, cells were incubated with medium alone (with no treatment). After 24 hours of treatment, the culture medium was replaced with a 0.5 mg mL^{-1} MTT solution prepared in RPMI 1640 culture medium. Following a 3 hour incubation at 37 °C with 5% CO_2, the MTT solution was removed, and pure DSMO was added to the wells. Absorbance was measured at λ = 540 nm using a BioTek Synergy H1 microplate reader (Agilent, USA).

2.9. Measurement of *S*-nitrosylated protein levels

The *S*-nitrosylated protein levels were measured in the FN1 cell line. For this purpose, FN1 cells were seeded at a density of 2.5 × 10^5 cells per well in six-well plates, with six wells allocated per experimental group (control, free GSNO at 250 μM, free GSNO at 500 μM, GSNO-CSNPs at 250 μM, and GSNO-CSNPs at 500 μM). The following day, the culture medium was replaced with fresh medium containing the appropriate concentrations of the treatments. After 24 hours of incubation at 37 °C in 5% CO_2, the medium was discarded, and cells were washed with 1 mL of phosphate-buffered saline (PBS). Cells were then harvested using a cell scraper and transferred to separate tubes. To lyse the cells, the suspensions were sonicated twice at 60% amplitude (Qsonica Q55 sonicator), with brief pauses between sonications to prevent overheating. The lysates were centrifuged at 480 G for 5 minutes using a centrifuge (Eppendorf MiniSpin). The supernatants were collected, and total protein content was determined by the Pierce BCA assay (Thermo Scientific), following the manufacturer's instructions. For the detection of *S*-nitroso-proteins, aliquots containing 300 μg of total protein were analyzed in a World Precision Instrument TBR-1025 system equipped with an ISO-NOP NO sensor. Before measurement, the sensor was stabilized in 0.1 M copper(II) chloride solution, which catalyzes the cleavage of S–NO bonds, thus liberating free NO.[48] The resulting signals were recorded using LabScribe 4.3 software.

2.10. Statistical analyses

Statistical analyses were performed using GraphPad Prism 8.0.2 (GraphPad Software) and Design-Expert 13 (Stat-Ease). In the Plackett–Burman design, statistical evaluation was based on the calculation of standardized effects to identify the most influential synthesis parameters, using Pareto charts and *p*-values (α = 0.1) to determine statistical significance. In the Face-Centered Design, mathematical models were constructed for each response variable when statistically appropriate. These models were evaluated using analysis of variance (ANOVA) to assess model significance, and multiple linear regression to estimate the contribution of each term. Model adequacy was verified through the coefficient of determination (R^2), adjusted R^2, predicted R^2, and the lack-of-fit test, ensuring reliability and predictive power within the experimental space. For biological assays and kinetic experiments, pairwise comparisons between groups were conducted using one-way ANOVA followed by Tukey's *post hoc* test, with statistical significance set at $p < 0.05$. All experiments were performed in at least triplicate, as specified in each figure caption, and results are reported as mean ± standard deviation.

3. Results and discussion

3.1. Plackett–Burman design for identifying key factors of the synthesis

A Plackett–Burman design was conducted to identify the factors that potentially influence the average diameter, PDI, ZP, and stability over time of GSH-CSNPs. Eight variables involved in the synthesis process were investigated for this purpose. The experimental matrix and the numerical results are detailed in Tables S1 and S2,† respectively.

3.1.1. Factors affecting the size, PDI, and ZP of GSH-CSNPs. In the first stage of the study, the initial DLS parameters were measured immediately post-synthesis for all nanoparticles produced according to the Plackett–Burman matrix. The standardized effects of each investigated factor were estimated, and the results are presented in Table 3.

As shown in Table 3, various factors influenced the average diameter, PDI, and ZP of the GSH-CSNPs immediately post-synthesis. Significant factors included the initial chitosan concentration, TPP solution concentration, CS : TPP mass ratio, final GSH concentration, initial acetic acid concentration, and ionic strength, all of which played key roles in determining these nanoparticle properties. In contrast, the rate of TPP addition and the pH of the TPP solution did not significantly affect the measured properties within the investigated range. The GSH-CSNPs exhibited an average diameter, PDI, and ZP ranging from 99 to 335 nm, 0.167 to 0.982, and +12.5 to +39.3 mV, respectively, highlighting the importance of precise control over synthesis parameters to achieve nanoparticles with properties suitable for biomedical applications.

Table 3 Standardized effects calculated for each factor investigated in the Plackett–Burman design (initial DLS parameters)

Factor		Standardized effects[a]		
		D (nm)	PDI	ZP (mV)
x_1	Initial chitosan concentration	**+102.8**	−0.03	−2.7
x_2	TPP solution concentration	**+48.7**	−0.08	+0.3
x_3	TPP solution addition rate	−11.7	−0.13	−1.9
x_4	pH of TPP solution	−21.7	−0.07	−0.3
x_5	CS : TPP mass ratio	**+51.5**	**+0.41**	**+13.6**
x_6	Final GSH concentration	−2.3	−0.04	**−5.7**
x_7	Initial acetic acid concentration	**−29.5**	−0.11	+4.5
x_8	Additional ionic strength	**+28.8**	−0.12	**−6.2**

[a] Effects with a *p*-value < 0, 1 were considered significant and are highlighted in bold; the curvature effect was not significant for any of the responses investigated; *D* = average diameter; PDI = polydispersity index; ZP = zeta potential.

The average diameter of the nanoparticles was influenced by the initial chitosan concentration, TPP solution concentration, CS : TPP mass ratio, initial acetic acid concentration, and ionic strength. When a more concentrated chitosan solution was used, the nanoparticles tended to be larger due to the increased availability of polymer chains, leading to more extensive cross-linking between chitosan and TPP, which resulted in the formation of larger structures. Similarly, a higher concentration of TPP led to larger nanoparticles, as the faster and less controlled cross-linking of chitosan chains occurred when more TPP was introduced per drop. Additionally, a higher CS : TPP mass ratio resulted in larger nanoparticles because the excess chitosan and lower TPP amount led to a less efficient cross-linking process, producing less compact particles. In contrast, a higher initial acetic acid concentration produced smaller nanoparticles, as the improved solubility of chitosan in acidic media facilitated a more controlled and gradual cross-linking process. Finally, an increase in ionic strength also resulted in larger nanoparticles, likely because the Cl^- ions neutralized some of the positive charges on the chitosan chains, reducing electrostatic repulsion and allowing for closer packing and aggregation. This led to a less controlled assembly, forming larger and potentially more irregular nanoparticles.

The PDI of the nanoparticles was influenced only by the CS : TPP mass ratio. When a higher CS : TPP mass ratio was used, the PDI of the resulting nanoparticles increased significantly. This is likely because the excess of chitosan relative to TPP led to less efficient and uneven cross-linking, resulting in a broader size distribution and greater variability in nanoparticle formation, also corroborating with the effect of this parameter on the average size.

The ZP of the nanoparticles was influenced by the CS : TPP mass ratio, final GSH concentration, and ionic strength. A higher CS : TPP mass ratio naturally resulted in more available positively charged amino groups from the chitosan, leading to an increase in ZP. This positive effect is expected, as the excess chitosan provided more surface charge for the nanoparticles. Conversely, the final GSH concentration had a negative effect on the ZP. The decrease in ZP caused by higher GSH concentrations suggests that GSH molecules were adsorbed onto the positively charged amino groups of the chitosan. This adsorption neutralized some of the surface charge, leading to a reduction in the overall ZP of the nanoparticles. Similarly, higher ionic strength also had a negative effect on the ZP. The presence of more ions in the solution likely screened the surface charges, reducing the electrostatic repulsion between nanoparticles and lowering the overall ZP.

3.1.2. Factors affecting the stability of GSH-CSNPs over time. To assess stability, DLS parameters of the produced nanoparticles were monitored over time at 1, 7, and 30 days post-synthesis, with the nanoparticles stored either at room temperature (20 °C) or under refrigeration (4 °C). The results were normalized relative to the initial values from each run of the Plackett–Burman design to account for any inherent variability in initial particle size and distribution between different experimental conditions. Normalization ensures a more accurate comparison of the stability trends by reducing the influence of initial differences and highlighting the true effects of the experimental variables over time.

The 7 day data were selected over the 30 day data due to significant aggregation observed at 30 days in some samples, as can be seen in Fig. S1,† indicated by high PDI values and highly inconsistent particle sizes. This aggregation compromised the reliability of DLS measurements and the representativeness of the samples. In contrast, the 7 day data provided clearer insights into the effects of the studied variables while maintaining sample integrity. Therefore, the 7 day data were selected and treated as a system response. The standardized effects of each investigated factor were estimated, and the results are presented in Table 4.

As shown in Table 4, various factors influenced the stability of the CSNPs over time, depending on the storage conditions. Significant changes in the average diameter and PDI were detected after 7 days post-synthesis. In contrast, the ZP did not exhibit significant variation due to the individual factors investigated in the experimental design. It is likely that the observed changes in the ZP, as depicted in Fig. S1,† are related to higher-order interaction effects that could not be captured by the Plackett–Burman Design. Nevertheless, ZP was not directly correlated with the overall stability of the CSNPs and is not the

Table 4 Standardized effects calculated for each factor investigated in the Plackett–Burman design (variations in DLS parameters after 7 days)

		Standardized effects[a]					
		Storage at 20 °C			Storage at 4 °C		
Factor		*D*	PDI	ZP	*D*	PDI	ZP
x_1	Initial chitosan concentration	+0.13	**+0.19**	+0.10	+0.23	**+0.27**	**+0.19**
x_2	TPP solution concentration	+0.22	**+0.45**	+0.07	+0.35	**+0.29**	+0.15
x_3	TPP solution addition rate	−0.16	−0.01	+0.15	−0.40	−0.06	+0.16
x_4	pH of TPP solution	+0.25	+0.13	−0.04	+0.44	**+0.26**	−0.02
x_5	CS : TPP mass ratio	**−0.49**	**−0.29**	+0.04	−0.42	−0.14	+0.12
x_6	Final GSH concentration	**−0.29**	**−0.26**	+0.04	**−0.52**	**−0.26**	+0.15
x_7	Initial acetic acid concentration	**−0.27**	+0.10	−0.02	**−0.63**	−0.01	−0.06
x_8	Additional ionic strength	+0.14	−0.12	+0.02	+0.33	−0.03	+0.10

[a] Effects with a *p*-value < 0.1 were considered significant and are highlighted in bold; the curvature effect was not significant for any of the responses investigated; *D* = average diameter; PDI = polydispersity index; ZP = zeta potential.

sole determinant of the stability of nanoparticles of this nature.

Biopolymeric nanoparticles produced using the ionotropic gelation method, such as CSNPs, are primarily subject to three destabilization mechanisms: aggregation, disaggregation, and rupture. Aggregation occurs when the surface charge of the nanoparticles is insufficient to maintain electrostatic repulsion, resulting in the formation of larger aggregates. Disaggregation refers to the process where previously formed aggregates or clusters of nanoparticles break apart into smaller, individual nanoparticles. Rupture, on the other hand, involves the fragmentation of nanoparticles into smaller particles due to structural instability. These destabilizing factors compromise the structural integrity of the nanoparticles, which may limit their effectiveness in biomedical applications.[49–51]

According to the data in Table 4, factors with a p-value < 0.1 that influenced the properties of the CSNPs under both storage conditions were considered significant. However, it is important to note that Plackett–Burman Designs may sometimes identify insignificant factors as significant due to their inherent limitations in statistical power and factor screening.[52] Therefore, it is essential to complement statistical analysis with consistency checks, such as assessing nanoparticle stability under various storage conditions, to validate the significance of the observed effects.

In this sense, the initial chitosan concentration and the TPP solution concentration used in the synthesis were identified as critical variables that promote the aggregation of GSH-CSNPs over time, both at room temperature and under refrigeration. The aggregation observed with higher TPP concentrations could be related to an excess of crosslinking agent added per drop of the TPP solution, leading to the immediate formation of local overly rigid structures that promote particle-particle interactions and eventual aggregation. Additionally, higher chitosan concentrations may contribute to increased viscosity during synthesis, which can hinder proper mixing and dispersion, resulting in uneven crosslinking and particle instability over time.

Conversely, the CS : TPP mass ratio, the final GSH concentration, and the initial acetic acid concentration were identified as factors related to nanoparticle rupture/disaggregation, leading to a decrease in average diameter, PDI, or both over time. The rupture/disaggregation observed with higher CS : TPP mass ratios is likely due to insufficient crosslinking of the chitosan chains, resulting in an unstable nanoparticle structure that becomes prone to rupture over time. The final GSH concentration may influence nanoparticle stability through GSH adsorption onto the surface of the chitosan chains, disrupting the intermolecular interactions necessary for maintaining nanoparticle integrity and possibly causing particle disintegration or disaggregation. Finally, the decrease in the PDI associated with higher initial acetic acid concentrations is likely due to the protonation of chitosan chains, which increases electrostatic repulsion between the aggregates formed during the early stages of synthesis. Additionally, partial decomposition of TPP in acidic conditions may further destabilize the nanoparticle structure, leading to rupture over time.

The storage temperature was found to significantly influence the stability of the nanoparticles over time. Nanoparticles stored at 4 °C exhibited greater variations in size, polydispersity index (PDI), and ZP compared to those stored at room temperature (20 °C) (Table 4). This behavior can be attributed to the reduced solubility of chitosan at lower temperatures, which may promote polymer precipitation and destabilize the colloidal suspension. Additionally, lower temperatures likely decrease particle kinetic energy, reducing electrostatic repulsion and increasing aggregation tendencies. Based on these observations, subsequent nanoparticles were stored at room temperature to ensure better stability and reproducibility of results.

3.2. Face-centered design for refinement and optimization

Based on the findings regarding the initial properties and stability of GSH-CSNPs over time, it was possible to adjust the synthesis parameters to produce smaller and more stable nanoparticles. Among the eight variables investigated, the CS : TPP mass ratio and the final GSH concentration were identified as critical factors and selected for further refinement and optimization through a Face-Centered Design. These factors were identified as the most significant among those studied in the Plackett–Burman Design. The CS : TPP mass ratio plays a crucial role in determining the average size, PDI, ZP, and long-term stability of the nanoparticles. Therefore, it was prioritized for its critical impact on GSH-CSNPs properties. Similarly, the final GSH concentration significantly influences key characteristics for biological activity, making its control essential for biomedical applications. Conversely, the other parameters were fixed at levels conducive to producing nanoparticles with smaller size and improved stability, targeting optimal properties for biomedical applications. Specifically, the initial chitosan concentration was set at 0.5% (w/v), the TPP solution concentration at 1 mg mL^{-1}, and the TPP addition rate at 0.1 mL min^{-1}. The pH of the TPP solution was left unadjusted, maintaining its natural pH of approximately 8–9. Additionally, the initial acetic acid concentration was fixed at 1.5% (w/v) to reduce nanoparticle size and PDI, and no additional ionic strength was introduced (*i.e.* absence of NaCl).

3.2.1. Effects of key synthesis parameters on initial properties and stability of GSH-CSNPs over time. Fig. 1 presents the contour plots derived from the statistical modeling of experimental data from the FCD, corresponding to the initial parameters of the GSH-CSNPs measured immediately post-synthesis. Only statistically significant terms ($p < 0.05$) were incorporated into the models. In addition, adequate values of R^2, R^2_{adj}, and standard deviations were obtained as can be seen in Table S5.† Also, all adjusted models accounted for the majority of observed variance within the design space, showing no lack of fit. Therefore, the obtained models can be used to explain

and predict how the initial properties of the GSH-CSNPs vary in function of the investigated synthesis variables.

The initial average diameter of GSH-CSNPs was influenced by both the CS : TPP mass ratio and the final GSH concentration. Although the final GSH concentration did not significantly impact the initial average diameter in the PB design, likely due to the wider range of concentrations tested, the refined analysis within the FCD space—offering higher statistical resolution and power—identified notable linear and quadratic effects for these variables. As shown in Fig. 2A, a lower CS : TPP mass ratio (1.5–2) combined with a higher final GSH concentration (30–35 mmol L^{-1}) can yield GSH-CSNPs with an optimal initial average size of approximately 100 nm. This size results from ideal crosslinking conditions and a controlled interaction between GSH molecules and chitosan chains. Similar effects were observed for the PDI of the GSH-CSNPs (Fig. 2B), where optimal conditions for lower PDIs were achieved with CS : TPP mass ratios below approximately 1.7 and final GSH concentrations between 27 and 37 mmol L^{-1}.

The ZP (Fig. 2C) was primarily influenced by the CS : TPP mass ratio. A higher CS : TPP mass ratio led to GSH-CSNPs with lower surface charges, as the positively charged amino groups of CS were neutralized by the negatively charged TPP molecules during crosslinking. Although an effect of final GSH concentration on ZP was noted in the PB design, with higher GSH concentrations correlating with a reduction in ZP (potentially due to GSH molecule adsorption on CS amino groups), the narrower range of GSH concentrations explored in the FCD

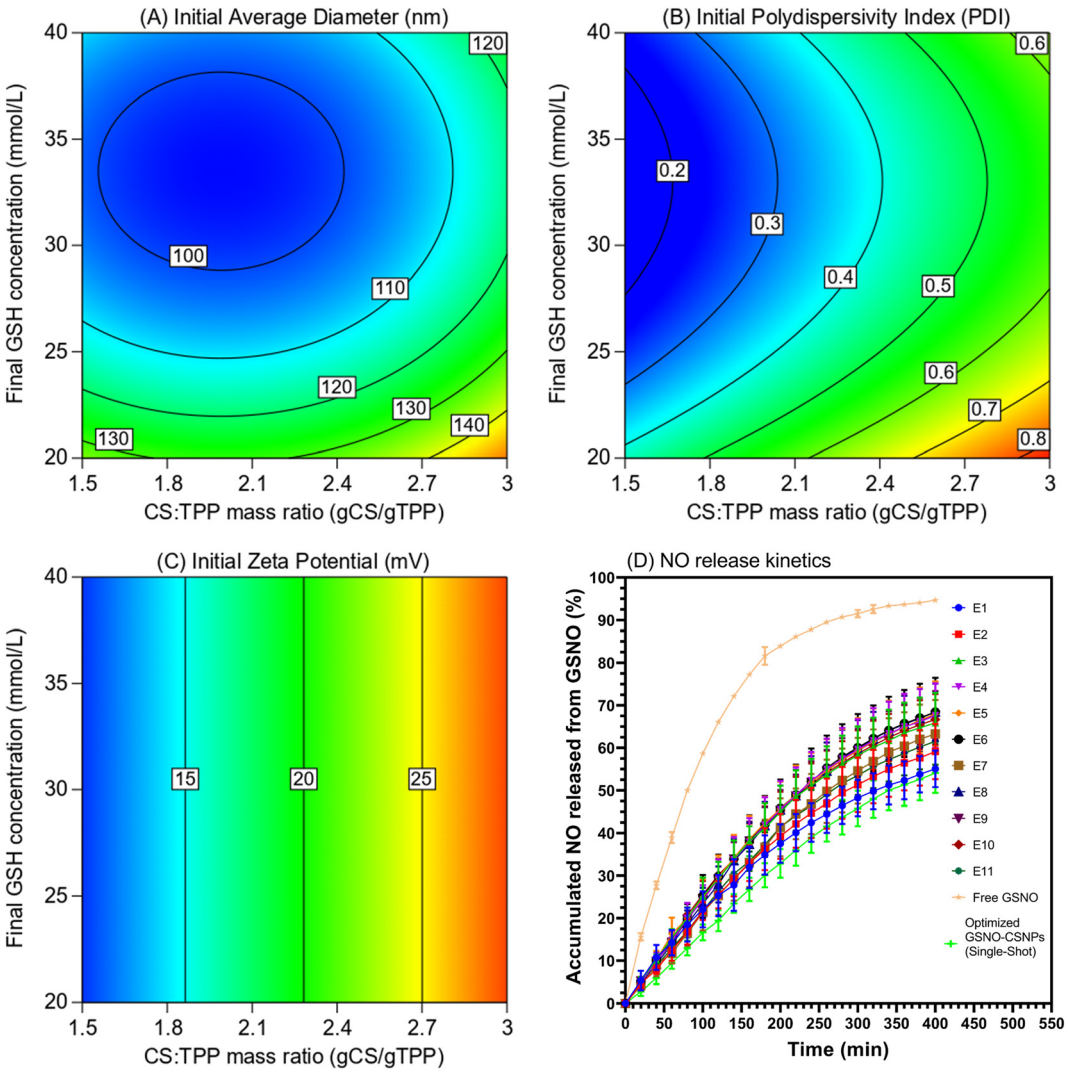

Fig. 2 Contour plots obtained in the Face-Centered Design for initial properties of GSH-CSNPs measured immediately post-synthesis and NO release kinetics from GSNO. (A) Effect of final GSH concentration and CS : TPP mass ratio on the initial average diameter of GSH-CSNPs; (B) effect of final GSH concentration and CS : TPP mass ratio on the initial polydispersity index (PDI) of GSH-CSNPs; (C) effect of final GSH concentration and CS : TPP mass ratio on the initial ZP of GSH-CSNPs; (D) NO release kinetic curves from GSNO at 37 °C for free GSNO, GSNO-CSNPs synthesized in the FCD, and the optimized GSNO-CSNPs. (E1–E11) GSNO-CSNPs produced in the FCD; (Free GSNO) GSNO in the absence of CSNPs; (optimized GSNO-CSNPs (single-shot)) optimized GSNO-CSNPs produced *via* single-shot methodology. Data obtained in triplicates.

(20–40 mmol L^{-1} in FCD *vs*. 20–100 mmol L^{-1} in PB) clarified that significant effects on ZP require substantial GSH concentration variations.

Regarding the stability of the GSH-CSNPs, models for the normalized stability indices of the CSNPs could not be established, as the variation in the data could not be adequately explained by the two variables investigated. In the Plackett–Burman design, variations of up to 250% were observed in the diameter, PDI, and ZP of the CSNPs after 7 days. After identifying the most influential parameters affecting these properties in the PB design and adjusting the synthesis conditions to minimize these effects—while fixing other parameters at optimized levels—variations in diameter, PDI, and ZP were reduced to approximately ±20% in the Face-Centered Design (FCD) experiments (Table S4†). Additionally, the CSNPs remained stable within these ±20% variations relative to their initial parameters after 30 days of storage at room temperature, further demonstrating the improved long-term stability achieved. This marked a significant improvement in nanoparticle stability. The remaining variability is likely attributed to random fluctuations, including batch-to-batch inconsistencies, measurement noise, and inherent stochastic processes in nanoparticle formation and aging.

3.2.2. Effects of key synthesis parameters on NO release kinetics from GSNO-CSNPs. The NO release kinetics from the GSNO-CSNPs produced in the FCD were evaluated by monitoring changes in the characteristic GSNO absorption band at 545 nm over 7 hours at 37 °C, mimicking physiological temperature. GSNO-CSNPs were obtained after nitrosation of GSH-CSNPs, as described previously in section 2.5. As depicted in Fig. 2D, free GSNO degraded significantly faster than the GSNO in the presence of CSNPs, likely due to the cage effect and the increased viscosity of the nanoparticle suspension, as previously reported.[53,54] The presence of the CSNPs creates a more confined microenvironment that restricts molecular permeation and limits GSNO degradation, and NO release, by reducing its direct interaction with surrounding aqueous components. Additionally, the increased viscosity of the medium further impedes the mobility of reactive species, slowing down the degradation process.[55,56] While more than 80% of GSNO degradation was observed for free GSNO within 200 minutes, the degradation in the presence of CSNPs was significantly lower, around 30–40%. On the other hand, no significant differences were observed among the kinetic profiles of the GSH-CSNPs synthesized in the FCD. The variations observed among the center points of the FCD (E9, E10, and E11) after 400 minutes ranged from approximately 52% to 72%. These replicates, synthesized under the same conditions, exhibited higher variability than that observed between different experimental groups, suggesting that the CS : TPP mass ratio and the final GSH concentration, the two variables investigated, did not significantly influence the GSNO degradation kinetics within the time range studied. Such variations are likely attributed to intrinsic random fluctuations during synthesis, rather than systematic effects of the tested parameters. The primary factor influencing the NO release rate in this case seems to be the initial concentration of *S*-nitrosothiol used during the kinetic experiments, as the degradation reaction of *S*-nitrosothiols typically follows a first-order kinetic profile.[57] Therefore, the results indicate that the CSNPs effectively prolongs NO release from GSNO, preventing an initial burst and ensuring a more sustained delivery of the active molecule over time for all the formulations tested in the FCD.

3.3. Production and characterization of optimal GSH-CSNPs

Based on the results obtained from the PBD and FCD, optimized nanoparticles were produced with the goal of achieving a reduced average hydrodynamic diameter and PDI, increased ZP, enhanced stability over time, and efficient reactant usage. To this end, GSH-CSNPs were synthesized under the following conditions: an initial chitosan concentration of 0.5% (w/v), a TPP solution concentration of 1 mg mL^{-1}, a TPP addition rate of 0.1 mL min^{-1}, and an unadjusted TPP solution pH (natural pH of approximately 8–9), a CS : TPP mass ratio of 1.5, and a Final GSH concentration of 30 mmol L^{-1}. The initial acetic acid concentration was set at 1.5% (w/v), no additional ionic strength was introduced (*i.e.*, absence of NaCl), and the nanoparticles were stored at room temperature. For comparison, since the TPP addition rate showed no significant effect in this study, GSH-CSNPs were also synthesized using a single-shot method, where the TPP solution was added all at once instead of through controlled addition. GSH was nitrosated, as previously described in the experimental section, leading to GSNO-CSNPs.

The predicted and experimental properties of the optimized GSH-CSNPs, as shown in Table 5, demonstrated strong agree-

Table 5 Predicted and experimental properties of optimized GSH-CSNPs

Property	Predicted	Optimized GSH-CSNPs	Optimized GSH-CSNPs (single-shot)
Initial average diameter (nm)	103.2 ± 7.4	90.2 ± 0.5	77.1 ± 1.5
Initial PDI	0.169 ± 0.096	0.269 ± 0.051	0.209 ± 0.010
Initial ZP (mV)	+10.6 ± 2.0	+16.2 ± 1.3	+15.3 ± 2.1
Average diameter 60 days post-synthesis (nm)[a]	—	98.3 ± 2.3	82.7 ± 2.1
PDI 60 days post-synthesis[a]	—	0.275 ± 0.052	0.212 ± 0.035
ZP 60 days post-synthesis (mV)[a]	—	+16.8 ± 2.3	+15.9 ± 1.7

[a] Storage at room temperature (20 °C).

ment with the values predicted by the statistical models based on the FCD data. Notably, GSH-CSNPs produced *via* the single-shot method exhibited slightly smaller sizes with a Gaussian size distribution (Fig. 3A), reduced PDI (Table 5), and sustained NO release from GSNO after nitrosation of GSH (Fig. 2D). A HRTEM image of the optimized GSH-CSNPs (single-shot), shown in Fig. 3B, revealed that the CSNPs exhibit a quasi-spherical shape in their dry form, also confirming the nanometric size of the particles. Furthermore, no substantial differences were observed in the average hydrodynamic size, PDI, or ZP after 60 days post-synthesis (Table 5), indicating excellent stability within the investigated time frame.

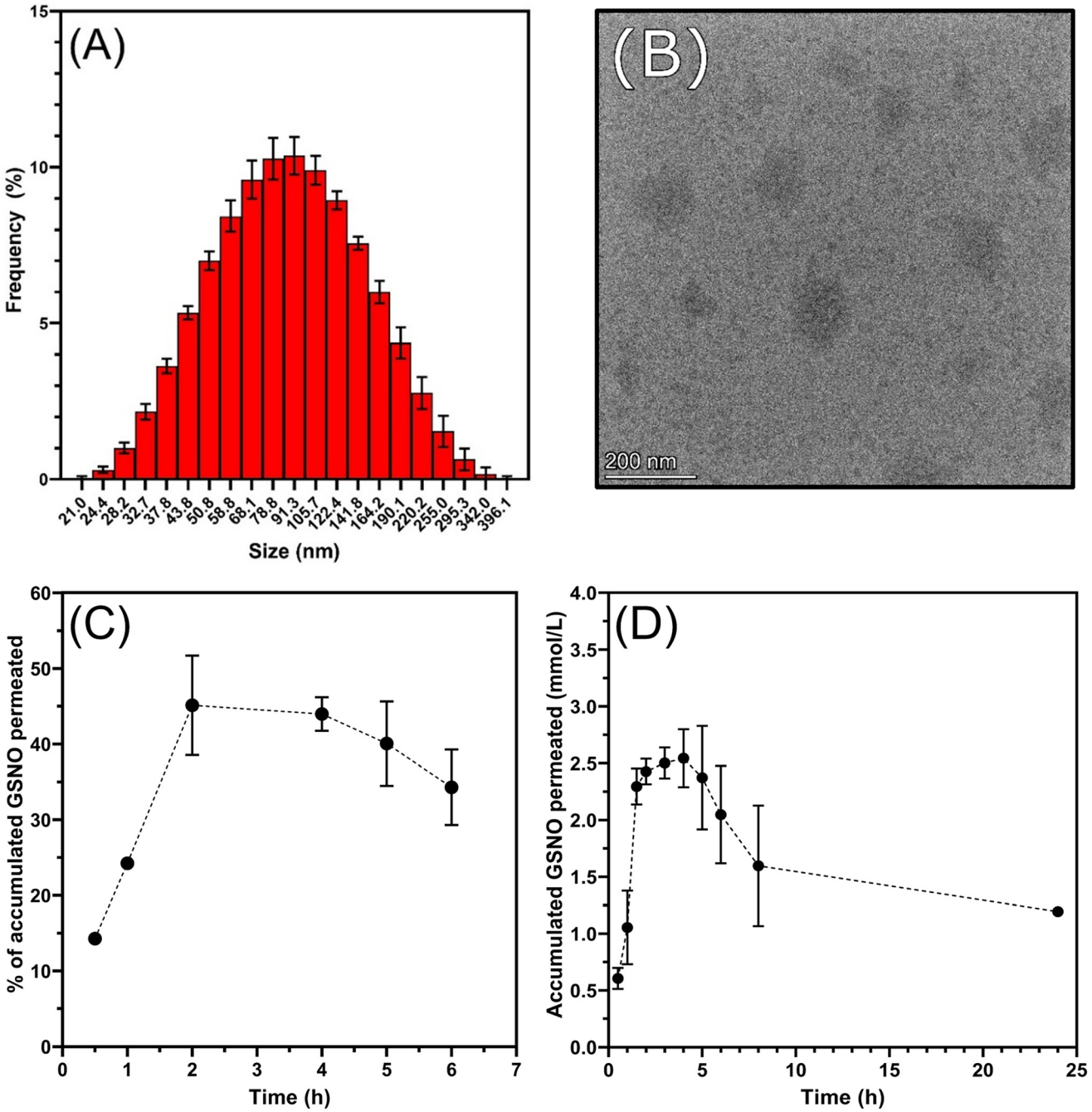

Fig. 3 Characterization data of optimized GSH-CSNPs synthesized *via* the single-shot method: (A) size distribution histogram obtained from DLS analysis; (B) HRTEM image illustrating the morphology of the synthesized GSH-CSNPs; (C) percentage of accumulated GSNO permeated through the Strat-M® membrane using Franz diffusion cells at 32.5 °C for 6 hours (initial GSNO concentration: 30 mmol L^{-1}); (D) accumulated GSNO concentration (mmol L^{-1}) permeated through the membrane over a 24 hour period. Data in (A), (C), and (D) represent mean ± standard deviation (n = 3)".

3.4. *In vitro* GSNO permeation assay

For the evaluation of the release profile of GSNO from CSNPs, a two-compartment system was used following the Franz permeation cell model. This setup allows for the controlled release of the drug or bioactive compound, simulating physiological conditions for topical administration until systemic absorption occurs. Fig. 3 presents the GSNO release profile at 32.5 °C (approximately the temperature of human skin) from the optimized GSNO-CSNPs synthesized *via* the single-shot method. The GSNO release was monitored over 24 hours, showing an initial burst release within the first 2 hours, followed by a gradual increase up to 4–5 hours. After this period, a decline in release was observed, which continued until the end of the experiment (24 hours). The GSNO release rate in the first 2 hours was 2.4 mmol L^{-1} h, while between 3 to 8 hours, it was 1.7 mmol L^{-1} h. A similar release profile was reported by Opländer *et al.*,[58] demonstrating an initial burst of NO release, suggesting that polymeric nanoparticles or controlled release systems could extend this release period.

The maximum amount of diffused GSNO through the membrane was 65.77 ± 3.82% of the initial concentration (30 mmol L^{-1}) within 4 hours. The incorporation of GSNO into polymeric nanoparticles was highlighted as the primary method for controlling the release of this bioactive compound. Several studies have demonstrated that free GSNO exhibits rapid action but suffers from extreme instability, reinforcing the necessity of encapsulation strategies to enhance its sustained release.[58–60]

The release profile of GSNO from the GSNO-CSNPs were evaluated using mathematical models, including first-order, Higuchi, Korsmeyer-Peppas, and Hixson & Crowell (Table 6). The Korsmeyer-Peppas model is particularly useful for analyzing release mechanisms when the underlying processes are not fully understood or when multiple mechanisms are involved. In this case, the release of GSNO appears to be governed by a combination of two primary processes: (1) drug transport following Fick's Law (diffusion) and (2) polymer matrix erosion. This is consistent with the behavior of polymeric matrices, such as chitosan, which exhibit chain relaxation over time. The relaxation of chitosan chains allows for rearrangement and energy dissipation, which is particularly relevant in controlled drug release applications, as it directly influences the release kinetics of the encapsulated drug. The release exponent (n) in the Korsmeyer-Peppas model provides insight into the dominant release mechanism. For spherical or cylindrical systems, values of $n \leq 0.45$ indicate Fickian transport mechanism, where drug release is primarily driven by concentration gradients. When $n = 0.89$, the release is controlled by polymer erosion (case II transport). For intermediate values ($0.45 < n < 0.89$), the release mechanism is considered anomalous, involving a combination of permeation and erosion processes.[61] In the case of GSNO release from CSNPs, the observed value of "$n \approx 0.29$" suggests a Fickian transport mechanism, indicating that drug release is primarily driven by diffusion due to concentration gradients. However, additional factors, such as polymer relaxation or interactions between GSNO and the chitosan matrix, may contribute to the release profile and warrant further investigation.

The results of release profile of GSNO from CS nanoparticles indicated that this system followed the Korsmeyer-Peppas model, exhibiting the highest release constant (K_{rel}) and the best correlation coefficient ($R^2 = 0.92$), as summarized in Table 6. In summary, the diffusion of GSNO from CS nanoparticles is a complex process is primarily driven by concentration gradients, consistent with a Fickian transport mechanism ($n \approx 0.29$). The Korsmeyer-Peppas model effectively describes this behavior, highlighting the importance of understanding the interplay between drug diffusion and polymer matrix properties, such as porosity and chemical interactions, for optimizing controlled drug delivery systems. Consistent with these results, Pelegrino *et al.*[62] demonstrated that encapsulating GSNO into CS nanoparticles (CSNPs) significantly extended its release profile compared to free GSNO, also with the two mathematical models were best fitted to the experimental data: the Higuchi and Korsmeyer-Peppas models. This extended release is particularly advantageous for biomedical applications, as it enables sustained NO delivery over prolonged periods, potentially enhancing therapeutic efficacy while reducing adverse effects. The mathematical models confirmed that the release process is primarily driven by diffusion, consistent with a Fickian transport mechanism, emphasizing the critical role of nanoparticle design in tailoring drug release kinetics. These insights highlight the potential of CS-based nanoparticles as effective carriers for controlled and sustained drug delivery.

3.5. Cell viability assay

The cytotoxicity assays were conducted using the human fibroblast FN1 cell line, which serves as a relevant *in vitro* model for evaluating the biocompatibility of nanomaterials intended for biomedical applications. Fibroblasts are the predominant type of cell in dermis and play a crucial role in wound healing, extracellular matrix production, and overall skin homeostasis, making them a reliable model for assessing potential cytotoxic effects of novel biomaterials before advancing to more complex biological systems.[63] The results obtained are shown in Fig. 4A.

Table 6 Release constants and determination coefficients obtained for GSNO permeation from chitosan nanoparticles

	First order		Hixson & Crowell		Higushi		Korsmeyer-Peppas		
Formulation	k_1 (%/h)	R^2	k_s (%/$h^{-0.3}$)	R^2	k_H (%/$h^{-1/2}$)	R^2	k_{KP} (%/h^{-n})	n	R^2
GSH-CSNPs	−2.8	0.34	0.082	0.47	37.25	0.80	23.87	0.29	0.92

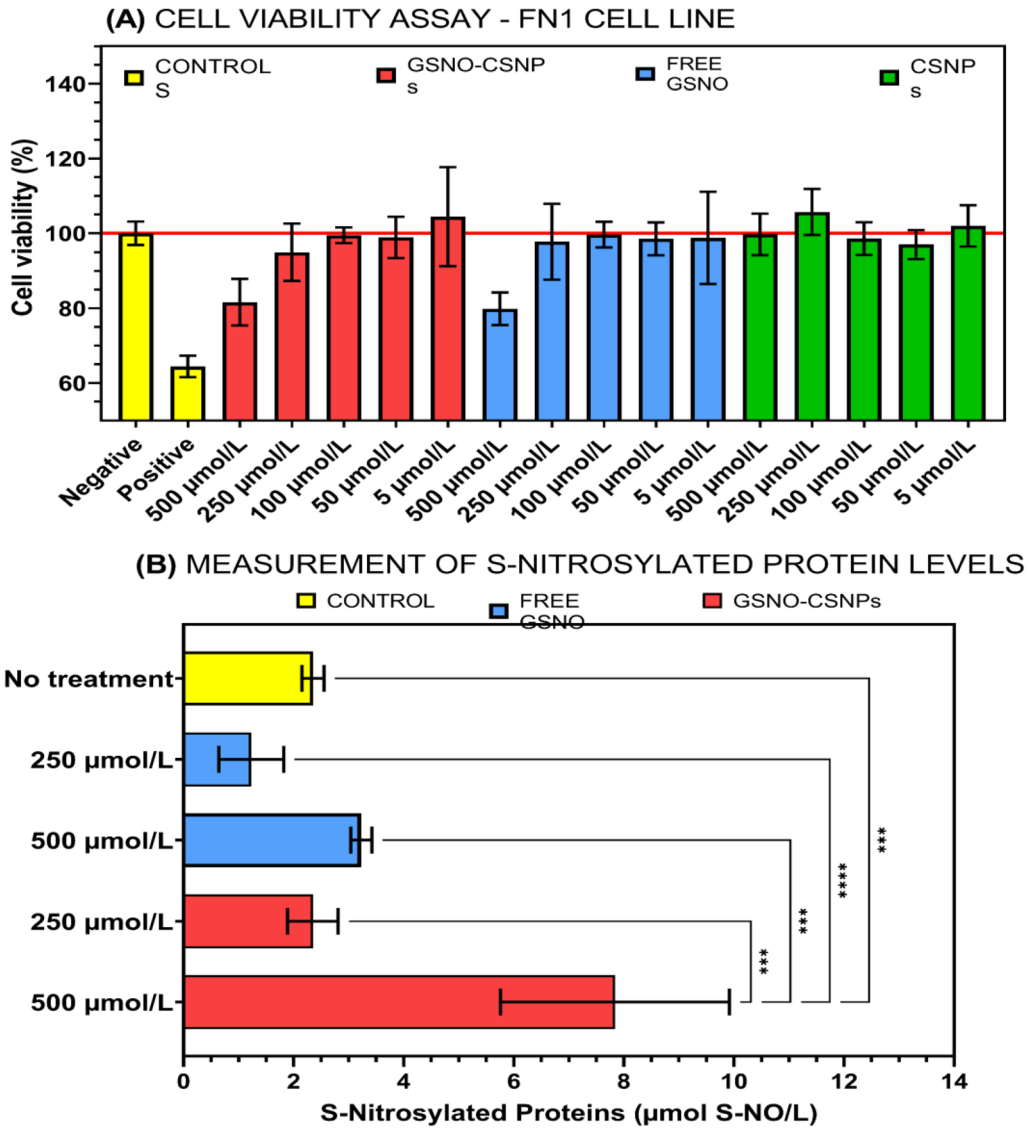

Fig. 4 Results of biological assays. (A) Cell viability assay for FN1 cells exposed to optimized NO-releasing chitosan nanoparticles (GSNO-CSNPs), free GSNO, and blank chitosan nanoparticles (CSNPs); (B) measurement of *S*-nitrosylated protein levels in FN1 cells exposed to selected doses of optimized NO-releasing chitosan nanoparticles (GSNO-CSNPs) and free GSNO. The "***" symbol in the figure indicates a statistically significant difference between the groups ($p < 0.05$). Data represent mean ± standard deviation ($n = 3$).

As can be seen in Fig. 4, blank CSNPs, synthesized without NO donors, exhibited no cytotoxicity signals, maintaining 100% cell viability up to 500 µmol L^{-1}. This finding highlights their excellent biocompatibility, reinforcing their potential as safe nanocarriers for biomedical applications, particularly in skin treatments where cytotoxic effects must be minimized. GSNO-CSNPs and free GSNO did not reduce cell viability up to 250 µmol L^{-1} in terms of the NO donor (GSNO), suggesting that the presence of the nanomaterial did not increase the cytotoxicity of the NO donor. Interestingly, GSNO-CSNPs and free GSNO exhibited no significant difference in their biological activity in the FN1 model, likely because fibroblasts possess moderate antioxidant defense mechanisms. Fibroblasts naturally regulate oxidative stress through intracellular antioxidant enzymes such as superoxide dismutase, catalase, and glutathione peroxidase, which modulate redox balance and may influence NO reactivity and availability before it can induce cytotoxic effects.[64–66] Therefore, the encapsulation process did not interfere with NO release in a way that alters its toxicity in the investigated fibroblast model, further supporting the potential of these nanoparticles as controlled NO delivery systems in dermatological applications.

In previous work,[67] NO-releasing CSNPs with NO donor in concentrations lower than 250 µmol L^{-1} exhibited potent cytotoxic effects against tumor cell lines, including HepG2 (human hepatocellular carcinoma), B16F10 (mouse melanoma), K562 (human chronic myeloid leukemia), and Lucena-1 (a vincristine-resistant K562 sub-line). Notably, these nanoparticles

showed significantly lower cytotoxicity toward Melan-A, a non-tumoral murine melanocyte cell line, compared to melanoma B16F10, suggesting a significant toxicity toward tumor cells. Also, this range of concentration of NO is correlated with antimicrobial activity in skin,[68] while lower NO concentrations can be employed for regenerative purposes, such as wound healing,[68,69] highlighting the potential of NO-releasing CSNPs in a wide spectrum of dermatological applications.

3.6. Measurement of *S*-nitrosylated protein levels

In cellular systems, NO plays a crucial role in post-translational modifications, particularly through *S*-nitrosylation, a process in which an NO group covalently binds to cysteine residues in proteins by the direct action of NO radicals or transnitrosylation reactions. This modification influences various signaling pathways, including those involved in cellular homeostasis and apoptosis.[70,71] Given the significance of these pathways, the extent of protein *S*-nitrosylation in the FN1 cell lineage under different treatment conditions was investigated. The selected concentrations of NO donor (free GSNO or GSNO encapsulated in CSNPs) were 250 and 500 μM, based on previous findings indicating a reduction in cell viability starting at 500 μM GSNO. Fig. 4B presents the levels of *S*-nitrosylated proteins measured in FN1 cells under different treatment conditions.

The only condition exhibiting a statistically significant increase in protein *S*-nitrosylation was the group treated with 500 μM GSNO-CSNPs. In this case, the mean levels of *S*-nitrosylated proteins were approximately 3–4 fold-higher than those observed in the other groups, including free GSNO at the same concentration. Nevertheless, this pronounced rise in protein *S*-nitrosation did not translate into increased cell death compared to the free GSNO group, as demonstrated in the cell viability assay (Fig. 4A). One plausible explanation is that CSNPs enhance the intracellular delivery of GSNO, leading to elevated protein *S*-nitrosylation without exceeding the damage threshold required to trigger more pronounced cytotoxicity. Factors such as the subcellular localization of NO release and cellular protective responses (*e.g.*, denitrosylation enzymes) may mitigate lethal effects even under conditions of elevated protein *S*-nitrosylation. Consequently, increased *S*-nitrosylation does not necessarily correlate with heightened cytotoxicity, highlighting the complexity of NO-mediated signaling and cellular homeostasis.[71,72] Studies have shown that chitosan-based carriers can facilitate more effective intracellular uptake of bioactive molecules by promoting electrostatic interactions with the cell membrane and enhancing endocytic pathways.[73] This property supports the idea that nanoparticles can deliver a higher load of GSNO inside the cell, thereby increasing *S*-nitrosylated protein levels through NO release or *S*-transnitrosation reactions involving GSNO molecules, without necessarily amplifying cell death pathways.

These findings underscore the potential of CSNPs as a viable NO delivery system, offering enhanced intracellular bioavailability while maintaining cellular viability. This highlights their promise as a strategic tool in biomedical applications where controlled NO release is crucial for therapeutic efficacy.

4. Conclusions

This study aimed to optimize, for the first time, the synthesis of nitric oxide-releasing chitosan nanoparticles (CSNPs) using a chemometric approach, with emphasis on controlling physicochemical properties, colloidal stability, and NO release profiles. Through multivariate modeling, we demonstrated how synthesis parameters influence key nanoparticle characteristics and provided a rational framework for the design of functional CSNPs tailored for biomedical applications. The multivariate experimental design investigated eight synthesis parameters, including chitosan concentration, crosslinking ratio, and pH, identifying the most critical factors influencing nanoparticle stability and NO release. This optimization led to highly stable and biocompatible nanoparticles with sustained NO release, particularly relevant for skin-related biomedical applications. The optimized nanoparticles exhibited a hydrodynamic diameter of 77.1 ± 1.5 nm, a low PDI of 0.209 ± 0.010, and a positive zeta potential, ensuring high colloidal stability. NO release kinetics demonstrated a prolonged and controlled release profile, significantly enhancing NO availability compared to free GSNO. Cytotoxicity assays confirmed their safety in non-tumoral fibroblasts (FN1) up to a concentration of GSNO of 250 μM, which is sufficient for a wide spectrum of dermatological applications. Additionally, quantification of *S*-nitrosylated proteins in FN1 cells revealed that GSNO-CSNPs at 500 μM significantly increased *S*-nitrosylation levels, approximately 3–4 fold higher than free GSNO at the same concentration, without causing additional cytotoxicity. This indicates that CSNPs effectively enhance intracellular GSNO delivery, promoting protein *S*-nitrosylation while preserving cell viability. Beyond optimizing synthesis parameters, this study provides a novel methodological framework for tailoring NO-releasing chitosan nanoparticles with precision, addressing key challenges in nanoparticle reproducibility and therapeutic efficacy. Unlike conventional approaches, the integration of chemometric modeling enables data-driven decision-making, ensuring scalable and reproducible synthesis while fine-tuning NO release characteristics. Future studies can focus on further *in vitro* evaluations, exploring their effects in different dermatological applications such as wound healing, antimicrobial activity, cancer treatment, and modulation of inflammatory responses. Additionally, efforts can be directed toward developing suitable delivery systems for these nanoparticles, such as hydrogels or incorporation into biomedical materials, to enhance their applicability and therapeutic potential. By integrating nanotechnology with data-driven optimization, this study highlights the power of chemometric strategies in advancing NO-based therapies, ensuring reproducibility, scalability, and enhanced therapeutic efficacy.

Author contributions

Renan S. Nunes: conceptualization, data curation, formal analysis, investigation, methodology, project administration, vali-

dation, visualization, writing – original draft, writing – review & editing. Victor D. P. Cinel: investigation, validation, writing – original draft, writing – review & editing. Joana C. Pieretti: investigation, validation, writing – original draft, writing – review & editing. Kelli F. Mariano: investigation, validation, writing – original draft, writing – review & editing. Roberta A. dos Reis: investigation, validation, writing – original draft, writing – review & editing. Morgana Halfeld: investigation, validation, writing – original draft. Amedea B. Seabra: conceptualization, funding acquisition, project administration, resources, supervision, writing – original draft, writing – review & editing.

Data availability

The data supporting this study have been included as part of the ESI.† Figures and tables cited in the manuscript are provided in a supplementary Word document, ensuring clarity and accessibility. Additionally, all numerical data used for generating plots and tables throughout the manuscript are available in an Excel file to facilitate easy access and reproducibility. These supplementary files allow for full transparency and support the reproducibility of our findings.

Conflicts of interest

The authors declare no conflict of interest.

Acknowledgements

The authors are thankful for the financial support from Coordenação de Aperfeiçoamento de Pessoal de Nível Superior – Brasil (CAPES) Finance Code 001 and 88881.711920/2022-01 (ABS). We are also thankful for financial support from CNPq (313117/2019-5 (ABS) and 405908/2022-9 (ABS)), and from São Paulo Research Foundation (FAPESP, grants 2022/14645-2 (ABS), 2024/12112-2 (ABS), 2024/04079-5 (RSN), 2020/03646-2 (JCP), 2024/20778-0 (MH), and 2023/16363-7 (RAR)).

References

1 H. Alimoradi, A. Thomas, D. D. B. Lyth, A. Barzegar-Fallah, S. S. Matikonda, A. B. Gamble and G. I. Giles, SMA-BmobaSNO: an intelligent photoresponsive nitric oxide releasing polymer for drug nanoencapsulation and targeted delivery, *Nanotechnology*, 2022, **33**, DOI: **10.1088/1361-6528/ac4eb0**.

2 J. M. Soni, M. N. Sardoiwala, S. R. Choudhury, S. S. Sharma and S. Karmakar, Melatonin-loaded chitosan nanoparticles endows nitric oxide synthase 2 mediated anti-inflammatory activity in inflammatory bowel disease model, *Mater. Sci. Eng., C*, 2021, **124**, 112038, DOI: **10.1016/j.msec.2021.112038**.

3 N. Hasan, W. Luthfiyah, J. Palungan, M. Ullah, A. Z. Mustopa, M. Nurfatwa, H. Irawan, U. Usmar, A. Putranto and J.-W. Yoo, Nitric oxide-releasing self-healing hydrogel for antibacterial and antibiofilm efficacy against polymicrobial infection, *Future Microbiol.*, 2024, **19**, 1559–1571, DOI: **10.1080/17460913.2024.2411817**.

4 C. A. Contreras Lancheros, M. T. Pelegrino, D. Kian, E. R. Tavares, P. M. Hiraiwa, S. Goldenberg, C. V. Nakamura, L. M. Yamauchi, P. Pinge-Filho, A. B. Seabra and S. F. Yamada-Ogatta, Selective Antiprotozoal Activity of Nitric Oxide-releasing Chitosan Nanoparticles Against Trypanosoma cruzi: Toxicity and Mechanisms of Action, *Curr. Pharm. Des.*, 2018, **24**, 830–839, DOI: **10.2174/1381612824666180209105625**.

5 H. Bai, Z. Ding, M. Jiang and D. Yao, Self-Healing Nanozyme Hydrogel with Nitric Oxide Production and Photothermal Effect to Promote Wound Healing, *ACS Appl. Nano Mater.*, 2024, **7**, 24477–24487, DOI: **10.1021/acsanm.4c04121**.

6 C.-Y. Chiu, L. P. N. Quirante, Y.-T. Hsu, D. Van Hong Thien, C.-H. Li and M.-H. Ho, Preparation of NO-Releasing electrospun chitosan nanofibrous scaffolds for osteoconduction, *Mater. Technol.*, 2023, **39**, DOI: **10.1080/10667857.2023.2286834**.

7 J. L. Georgii, T. P. Amadeu, A. B. Seabra, M. G. de Oliveira and A. Monte-Alto-Costa, Topical S-nitrosoglutathione-releasing hydrogel improves healing of rat ischaemic wounds, *J. Tissue Eng. Regener. Med.*, 2011, **5**, 612–619, DOI: **10.1002/term.353**.

8 G. Li, K. Lv, Q. Cheng, H. Xing, W. Xue, W. Zhang, Q. Lin and D. Ma, Enhanced Bacterial–Infected Wound Healing by Nitric Oxide–Releasing Topological Supramolecular Nanocarriers with Self–Optimized Cooperative Multi–Point Anchoring, *Adv. Sci.*, 2023, **10**, 2206959, DOI: **10.1002/advs.202206959**.

9 J. C. Pieretti, B. M. Freire, G. M. Armentano, B. D. M. Santana, B. L. Batista, M. S. Carneiro-Ramos and A. B. Seabra, Chronic exposure to nitric oxide sensitizes prostate cancer cells and improved ZnO/CisPt NPs cytotoxicity and selectivity, *Int. J. Pharm.*, 2023, **640**, 122998, DOI: **10.1016/j.ijpharm.2023.122998**.

10 B. de Melo Santana, J. C. Pieretti, R. N. Gomes, G. Cerchiaro and A. B. Seabra, Cytotoxicity towards Breast Cancer Cells of Pluronic F-127/Hyaluronic Acid Hydrogel Containing Nitric Oxide Donor and Silica Nanoparticles Loaded with Cisplatin, *Pharmaceutics*, 2022, **14**, 2837, DOI: **10.3390/pharmaceutics14122837**.

11 L. J. Ignarro, Nitric oxide is not just blowing in the wind, *Br. J. Pharmacol.*, 2019, **176**, 131–134, DOI: **10.1111/bph.14540**.

12 J. C. Pieretti, M. T. Pelegrino, A. Boudier and A. B. Seabra, Recent progress in the toxicity of nitric oxide-releasing nanomaterials, *Mater. Adv.*, 2021, **2**, 7530–7542, DOI: **10.1039/D1MA00532D**.

13 G. da Silva, M. da Silva, D. Nascimento, E. Lima Silva, F. Gouvêa, L. de França Lopes, A. Araújo, K. Ferraz Pereira

and T. de Queiroz, Nitric Oxide as a Central Molecule in Hypertension: Focus on the Vasorelaxant Activity of New Nitric Oxide Donors, *Biology*, 2021, **10**, 1041, DOI: **10.3390/biology10101041**.

14 M. C. Cabello and A. R. Lippert, Development of a solid-supported light-triggered nitric oxide donor, *J. Photochem. Photobiol., A*, 2024, **450**, 115466, DOI: **10.1016/j.jphotochem.2024.115466**.

15 N. Naghavi, A. de Mel, O. S. Alavijeh, B. G. Cousins and A. M. Seifalian, Nitric Oxide Donors for Cardiovascular Implant Applications, *Small*, 2013, **9**, 22–35, DOI: **10.1002/smll.201200458**.

16 P. G. Wang, M. Xian, X. Tang, X. Wu, Z. Wen, T. Cai and A. J. Janczuk, Nitric Oxide Donors: Chemical Activities and Biological Applications, *Chem. Rev.*, 2002, **102**, 1091–1134, DOI: **10.1021/cr000040l**.

17 A. B. Seabra, E. Pankotai, M. Fehér, Á. Somlai, L. Kiss, L. Bíró, C. Szabó, M. Kollai, M. G. de Oliveira and Z. Lacza, S-nitrosoglutathione-containing hydrogel increases dermal blood flow in streptozotocin-induced diabetic rats, *Br. J. Dermatol.*, 2007, **156**, 814–818, DOI: **10.1111/j.1365-2133.2006.07718.x**.

18 J. L. Georgii, T. P. Amadeu, A. B. Seabra, M. G. de Oliveira and A. Monte-Alto-Costa, Topical S-nitrosoglutathione-releasing hydrogel improves healing of rat ischaemic wounds, *J. Tissue Eng. Regener. Med.*, 2011, **5**, 612–619, DOI: **10.1002/term.353**.

19 A. B. Seabra, J. C. Pieretti, B. de Melo Santana, M. Horue, G. R. Tortella and G. R. Castro, Pharmacological applications of nitric oxide-releasing biomaterials in human skin, *Int. J. Pharm.*, 2023, **630**, 122465, DOI: **10.1016/j.ijpharm.2022.122465**.

20 S. Abdel Azim, C. Whiting and A. J. Friedman, Applications of nitric oxide-releasing nanomaterials in dermatology: Skin infections and wound healing, *Nitric Oxide*, 2024, **146**, 10–18, DOI: **10.1016/j.niox.2024.03.001**.

21 H. Ming, K. Zhang, S. Ge, Y. Shi, C. Du, X. Guo and L. Zhang, A Mini Review of S-Nitrosoglutathione Loaded Nano/Micro-Formulation Strategies, *Nanomaterials*, 2023, **13**, 224, DOI: **10.3390/nano13020224**.

22 J. C. Pieretti, M. T. Pelegrino, N. M. Silveira, M. G. Rodrigues and A. B. Seabra, State-of-the-Art and Perspectives for Nanomaterials Combined with Nitric Oxide Donors: From Biomedical to Agricultural Applications, *ACS Appl. Nano Mater.*, 2024, 7, 18590–18609, DOI: **10.1021/acsanm.3c03482**.

23 F. V. Cabral, M. T. Pelegrino, I. P. Sauter, A. B. Seabra, M. Cortez and M. S. Ribeiro, Nitric oxide-loaded chitosan nanoparticles as an innovative antileishmanial platform, *Nitric Oxide*, 2019, **93**, 25–33, DOI: **10.1016/j.niox.2019.09.007**.

24 F. V. Cabral, M. T. Pelegrino, A. B. Seabra and M. S. Ribeiro, Nitric-oxide releasing chitosan nanoparticles towards effective treatment of cutaneous leishmaniasis, *Nitric Oxide*, 2021, **113–114**, 31–38, DOI: **10.1016/j.niox.2021.04.008**.

25 C. A. Contreras Lancheros, M. T. Pelegrino, D. Kian, E. R. Tavares, P. M. Hiraiwa, S. Goldenberg, C. V. Nakamura, L. M. Yamauchi, P. Pinge-Filho, A. B. Seabra and S. F. Yamada-Ogatta, Selective Antiprotozoal Activity of Nitric Oxide-releasing Chitosan Nanoparticles Against Trypanosoma cruzi: Toxicity and Mechanisms of Action, *Curr. Pharm. Des.*, 2018, **24**, 830–839, DOI: **10.2174/1381612824666180209105625**.

26 M. T. Pelegrino, J. C. Pieretti, G. Nakazato, M. C. Gonçalves, J. C. Moreira and A. B. Seabra, Chitosan chemically modified to deliver nitric oxide with high antibacterial activity, *Nitric Oxide*, 2021, **106**, 24–34, DOI: **10.1016/j.niox.2020.10.003**.

27 M. T. Pelegrino, R. B. Weller, X. Chen, J. S. Bernardes and A. B. Seabra, Chitosan nanoparticles for nitric oxide delivery in human skin, *MedChemComm*, 2017, **8**, 713–719, DOI: **10.1039/C6MD00502K**.

28 N. Hussain, Regulatory aspects in the pharmaceutical development of nanoparticle drug delivery systems designed to cross the intestinal epithelium and M-cells, *Int. J. Pharm.*, 2016, **514**, 15–23, DOI: **10.1016/j.ijpharm.2016.07.053**.

29 R. Priya, G. Rajivgandhi, T. Muneeswaran, S. Y. Nam, W.-S. Cho and M. Maruthupandy, Regulatory status and toxicological, environmental, and health impacts of chitosan nanoparticles, in *Fundamentals and Biomedical Applications of Chitosan Nanoparticles*, Elsevier, 2025, pp. 679–708. DOI: **10.1016/B978-0-443-14088-4.00013-7**.

30 T. I. Ramos, C. A. Villacis-Aguirre, K. V. López-Aguilar, L. Santiago Padilla, C. Altamirano, J. R. Toledo and N. Santiago Vispo, The Hitchhiker's Guide to Human Therapeutic Nanoparticle Development, *Pharmaceutics*, 2022, **14**, 247, DOI: **10.3390/pharmaceutics14020247**.

31 N. Tiwari, E. R. Osorio-Blanco, A. Sonzogni, D. Esporrín-Ubieto, H. Wang and M. Calderón, Nanocarriers for Skin Applications: Where Do We Stand?, *Angew. Chem., Int. Ed.*, 2022, **61**, e202107960, DOI: **10.1002/anie.202107960**.

32 Y.-N. Fan, G. Zhao, Y. Zhang, Q.-N. Ye, Y.-Q. Sun, S. Shen, Y. Liu, C.-F. Xu and J. Wang, Progress in nanoparticle-based regulation of immune cells, *Med. Rev.*, 2023, **3**, 152–179, DOI: **10.1515/mr-2022-0047**.

33 S. Fernandes, M. Quattrociocchi, M. Cassani, G. Savazzi, D. Johnson, G. Forte, F. Caruso and F. Cavalieri, Antibody-Free Glycogen Nanoparticles Engage Human Immune T Cells for Intracellular Delivery of Small Drugs or mRNA, *ACS Nano*, 2024, **18**, 28910–28923, DOI: **10.1021/acsnano.4c09156**.

34 A. Khan, K. J. Naquvi, M. F. Haider and M. A. Khan, Quality by design- newer technique for pharmaceutical product development, *Intell. Pharm.*, 2024, **2**, 122–129, DOI: **10.1016/j.ipha.2023.10.004**.

35 A. Kasemiire, H. T. Avohou, C. De Bleye, P. Y. Sacre, E. Dumont, P. Hubert and E. Ziemons, Design of experiments and design space approaches in the pharmaceutical bioprocess optimization, *Eur. J. Pharm. Biopharm.*, 2021, **166**, 144–154, DOI: **10.1016/j.ejpb.2021.06.004**.

36 A. Khan, K. J. Naquvi, M. F. Haider and M. A. Khan, Quality by design- newer technique for pharmaceutical product development, *Intell. Pharm.*, 2024, **2**, 122–129, DOI: 10.1016/j.ipha.2023.10.004.

37 L. Gurba-Bryśkiewicz, W. Maruszak, D. A. Smuga, K. Dubiel and M. Wieczorek, Quality by Design (QbD) and Design of Experiments (DOE) as a Strategy for Tuning Lipid Nanoparticle Formulations for RNA Delivery, *Biomedicines*, 2023, **11**, 2752, DOI: 10.3390/biomedicines11102752.

38 D. G. Gomes, T. V. Debiasi, M. T. Pelegrino, R. M. Pereira, G. Ondrasek, B. L. Batista, A. B. Seabra and H. C. Oliveira, Soil Treatment with Nitric Oxide-Releasing Chitosan Nanoparticles Protects the Root System and Promotes the Growth of Soybean Plants under Copper Stress, *Plants*, 2022, **11**, 3245, DOI: 10.3390/plants11233245.

39 E. M. A. Hejjaji, A. M. Smith and G. A. Morris, Evaluation of the mucoadhesive properties of chitosan nanoparticles prepared using different chitosan to tripolyphosphate (CS: TPP) ratios, *Int. J. Biol. Macromol.*, 2018, **120**, 1610–1617, DOI: 10.1016/j.ijbiomac.2018.09.185.

40 H. Jonassen, A.-L. Kjøniksen and M. Hiorth, Effects of ionic strength on the size and compactness of chitosan nanoparticles, *Colloid Polym. Sci.*, 2012, **290**, 919–929, DOI: 10.1007/s00396-012-2604-3.

41 H. Jonassen, A.-L. Kjøniksen and M. Hiorth, Stability of Chitosan Nanoparticles Cross-Linked with Tripolyphosphate, *Biomacromolecules*, 2012, **13**, 3747–3756, DOI: 10.1021/bm301207a.

42 W. Fan, W. Yan, Z. Xu and H. Ni, Formation mechanism of monodisperse, low molecular weight chitosan nanoparticles by ionic gelation technique, *Colloids Surf., B*, 2012, **90**, 21–27, DOI: 10.1016/j.colsurfb.2011.09.042.

43 N. Sawtarie, Y. Cai and Y. Lapitsky, Preparation of chitosan/tripolyphosphate nanoparticles with highly tunable size and low polydispersity, *Colloids Surf., B*, 2017, **157**, 110–117, DOI: 10.1016/j.colsurfb.2017.05.055.

44 M. T. Pelegrino, L. C. Silva, C. M. Watashi, P. S. Haddad, T. Rodrigues and A. B. Seabra, Nitric oxide-releasing nanoparticles: synthesis, characterization, and cytotoxicity to tumorigenic cells, *J. Nanopart. Res.*, 2017, **19**, 57, DOI: 10.1007/s11051-017-3747-4.

45 S. M. Shishido, A. B. Seabra, W. Loh and M. G. de Oliveira, Thermal and photochemical nitric oxide release from S-nitrosothiols incorporated in Pluronic F127 gel: potential uses for local and controlled nitric oxide release, *Biomaterials*, 2003, **24**, 3543–3553, DOI: 10.1016/S0142-9612(03)00153-4.

46 M. T. Pelegrino, D. R. de Araújo and A. B. Seabra, S-nitrosoglutathione-containing chitosan nanoparticles dispersed in Pluronic F-127 hydrogel: Potential uses in topical applications, *J. Drug Delivery Sci. Technol.*, 2018, **43**, 211–220, DOI: 10.1016/j.jddst.2017.10.016.

47 F. V. Cabral, B. D. M. Santana, C. N. Lange, B. L. Batista, A. B. Seabra and M. S. Ribeiro, Pluronic F-127 Hydrogels Containing Copper Oxide Nanoparticles and a Nitric Oxide Donor to Treat Skin Cancer, *Pharmaceutics*, 2023, **15**, 1971, DOI: 10.3390/pharmaceutics15071971.

48 J. C. Pieretti, B. M. Freire, G. M. Armentano, B. D. M. Santana, B. L. Batista, M. S. Carneiro-Ramos and A. B. Seabra, Chronic exposure to nitric oxide sensitizes prostate cancer cells and improved ZnO/CisPt NPs cytotoxicity and selectivity, *Int. J. Pharm.*, 2023, **640**, 122998, DOI: 10.1016/j.ijpharm.2023.122998.

49 Q. Dai, X. Zhu, J. Yu, E. Karangwa, S. Xia, X. Zhang and C. Jia, Mechanism of Formation and Stabilization of Nanoparticles Produced by Heating Electrostatic Complexes of WPI–Dextran Conjugate and Chondroitin Sulfate, *J. Agric. Food Chem.*, 2016, **64**, 5539–5548, DOI: 10.1021/acs.jafc.6b01213.

50 P. Sacco, S. Paoletti, M. Cok, F. Asaro, M. Abrami, M. Grassi and I. Donati, Insight into the ionotropic gelation of chitosan using tripolyphosphate and pyrophosphate as cross-linkers, *Int. J. Biol. Macromol.*, 2016, **92**, 476–483, DOI: 10.1016/j.ijbiomac.2016.07.056.

51 E. N. Koukaras, S. A. Papadimitriou, D. N. Bikiaris and G. E. Froudakis, Insight on the Formation of Chitosan Nanoparticles through Ionotropic Gelation with Tripolyphosphate, *Mol. Pharm.*, 2012, **9**, 2856–2862, DOI: 10.1021/mp300162j.

52 M. I. Rodrigues and A. F. Iemma, in *Experimental Design and Process Optimization*, CRC Press, 2014. DOI: 10.1201/b17848.

53 M. T. Pelegrino, L. C. Silva, C. M. Watashi, P. S. Haddad, T. Rodrigues and A. B. Seabra, Nitric oxide-releasing nanoparticles: synthesis, characterization, and cytotoxicity to tumorigenic cells, *J. Nanopart. Res.*, 2017, **19**, 57, DOI: 10.1007/s11051-017-3747-4.

54 M. T. Pelegrino, L. C. Silva, C. M. Watashi, P. S. Haddad, T. Rodrigues and A. B. Seabra, Nitric oxide-releasing nanoparticles: synthesis, characterization, and cytotoxicity to tumorigenic cells, *J. Nanopart. Res.*, 2017, **19**, 57, DOI: 10.1007/s11051-017-3747-4.

55 X. Niu, J. Cao, Y. Zhang, X. Gao, M. Cheng, Y. Liu, W. Wang and Z. Yuan, A glutathione responsive nitric oxide release system based on charge-reversal chitosan nanoparticles for enhancing synergistic effect against multidrug resistance tumor, *Nanomedicine*, 2019, **20**, 102015, DOI: 10.1016/j.nano.2019.102015.

56 M. Choi, N. Hasan, J. Cao, J. Lee, S. P. Hlaing and J.-W. Yoo, Chitosan-based nitric oxide-releasing dressing for anti-biofilm and in vivo healing activities in MRSA biofilm-infected wounds, *Int. J. Biol. Macromol.*, 2020, **142**, 680–692, DOI: 10.1016/j.ijbiomac.2019.10.009.

57 D. R. Noble and D. L. H. Williams, Structure–Reactivity Studies of the Cu2+-Catalyzed Decomposition of Four S-Nitrosothiols Based around the S-Nitrosocysteine/S-Nitrosoglutathione Structures, *Nitric Oxide*, 2000, **4**, 392–398, DOI: 10.1006/niox.2000.0291.

58 C. Opländer, T. Müller, M. Baschin, A. Bozkurt, G. Grieb, J. Windolf, N. Pallua and C. V. Suschek, Characterization of novel nitrite-based nitric oxide generating delivery systems

for topical dermal application, *Nitric Oxide*, 2013, **28**, 24–32, DOI: 10.1016/j.niox.2012.09.003.

59 F. V. Cabral, B. D. M. Santana, C. N. Lange, B. L. Batista, A. B. Seabra and M. S. Ribeiro, Pluronic F-127 Hydrogels Containing Copper Oxide Nanoparticles and a Nitric Oxide Donor to Treat Skin Cancer, *Pharmaceutics*, 2023, **15**, 1971, DOI: 10.3390/pharmaceutics15071971.

60 M. T. Pelegrino, B. De Araujo Lima, M. H. M. Do Nascimento, C. B. Lombello, M. Brocchi and A. B. Seabra, Biocompatible and Antibacterial Nitric Oxide-Releasing Pluronic F-127/Chitosan Hydrogel for Topical Applications, *Polymers*, 2018, **10**, 452, DOI: 10.3390/polym10040452.

61 A. Haq, B. Goodyear, D. Ameen, V. Joshi and B. Michniak-Kohn, Strat-M® synthetic membrane: Permeability comparison to human cadaver skin, *Int. J. Pharm.*, 2018, **547**, 432–437, DOI: 10.1016/j.ijpharm.2018.06.012.

62 M. T. Pelegrino, D. R. de Araújo and A. B. Seabra, S-nitrosoglutathione-containing chitosan nanoparticles dispersed in Pluronic F-127 hydrogel: Potential uses in topical applications, *J. Drug Delivery Sci. Technol.*, 2018, **43**, 211–220, DOI: 10.1016/j.jddst.2017.10.016.

63 V. Buranasudja, C. Muangnoi, K. Sanookpan, H. Halim, B. Sritularak and P. Rojsitthisak, Eriodictyol Attenuates H_2O_2-Induced Oxidative Damage in Human Dermal Fibroblasts through Enhanced Capacity of Antioxidant Machinery, *Nutrients*, 2022, **14**, 2553, DOI: 10.3390/nu14122553.

64 A. Moysan, I. Marquis, F. Gaboriau, R. Santus, L. Dubertret and P. Morlière, Ultraviolet A – Induced Lipid Peroxidation and Antioxidant Defense Systems in Cultured Human Skin Fibroblasts, *J. Invest. Dermatol.*, 1993, **100**, 692–698, DOI: 10.1111/1523-1747.ep12472352.

65 M. Deng, T. Z. Yu, D. Li, X. Wang, G. Zhou, W. Liu, Y. Cao, W. Xia, W. Li and W. J. Zhang, Human umbilical cord mesenchymal stem cell-derived and dermal fibroblast-derived extracellular vesicles protect dermal fibroblasts from ultraviolet radiation-induced photoaging in vitro, *Photochem. Photobiol. Sci.*, 2020, **19**, 406–414, DOI: 10.1039/c9pp00421a.

66 V. Buranasudja, C. Muangnoi, K. Sanookpan, H. Halim, B. Sritularak and P. Rojsitthisak, Eriodictyol Attenuates H_2O_2-Induced Oxidative Damage in Human Dermal Fibroblasts through Enhanced Capacity of Antioxidant Machinery, *Nutrients*, 2022, **14**, 2553, DOI: 10.3390/nu14122553.

67 M. T. Pelegrino, L. C. Silva, C. M. Watashi, P. S. Haddad, T. Rodrigues and A. B. Seabra, Nitric oxide-releasing nanoparticles: synthesis, characterization, and cytotoxicity to tumorigenic cells, *J. Nanopart. Res.*, 2017, **19**, 57, DOI: 10.1007/s11051-017-3747-4.

68 S. Abdel Azim, C. Whiting and A. J. Friedman, Applications of nitric oxide-releasing nanomaterials in dermatology: Skin infections and wound healing, *Nitric Oxide*, 2024, **146**, 10–18, DOI: 10.1016/j.niox.2024.03.001.

69 H. Yang, Q. Chen, H. Qiang, B. Wang, J. Chen, Y. Xie, L. Peng, H. Zhao and J. Tian, Corrole-based photothermal nanocomposite hydrogel with nitric oxide release for diabetic wound healing, *Acta Biomater.*, 2025, **192**, 431–445, DOI: 10.1016/j.actbio.2024.12.020.

70 T. Nakamura and S. A. Lipton, Emerging role of protein-protein transnitrosylation in cell signaling pathways, *Antioxid. Redox Signal.*, 2013, **18**, 239–249, DOI: 10.1089/ars.2012.4703.

71 D. T. Hess, A. Matsumoto, S.-O. Kim, H. E. Marshall and J. S. Stamler, Protein S-nitrosylation: purview and parameters, *Nat. Rev. Mol. Cell Biol.*, 2005, **6**, 150–166, DOI: 10.1038/nrm1569.

72 J. S. Stamler, S. Lamas and F. C. Fang, Nitrosylation, *Cell*, 2001, **106**, 675–683, DOI: 10.1016/S0092-8674(01)00495-0.

73 N. Aibani, R. Rai, P. Patel, G. Cuddihy and E. K. Wasan, Chitosan Nanoparticles at the Biological Interface: Implications for Drug Delivery, *Pharmaceutics*, 2021, **13**, 1686, DOI: 10.3390/pharmaceutics13101686.

